




Pressure-induced ferroelectric transition in LiBC

Hu Zhang ^{*}, Lulu Zhao, Chendong Jin , Ruqian Lian, Peng-Lai Gong, RuiNing Wang, JiangLong Wang, and Xing-Qiang Shi 

Key Laboratory of Optic-Electronic Information and Materials of Hebei Province, Institute of Life Science and Green Development, College of Physics Science and Technology, Hebei University, Baoding 071002, People's Republic of China



(Received 22 August 2022; revised 22 October 2022; accepted 7 November 2022; published 14 November 2022)

Ferroelectricity is usually suppressed by pressure. Here, we establish a general phenomenological theory to describe pressure-induced ferroelectrics and then relate it to real materials. Based on first-principles calculations, we identify a pressure-induced ferroelectric transition in which the nonpolar LiBC in the ZrBeSi structure type transforms into the polar state in the LiGaGe structure type at about 108 GPa. The pressure-induced ferroelectric LiBC has a larger polarization of 1.95 C/m² and band gap of 3.27 eV at 110 GPa. A ferroelectric multiple-well energy as a function of polar distortion is found. The pressure-induced ferroelectric transition is driven by the softness of one of the A_{2u} modes in the nonpolar LiBC above 60 GPa. We also find an enhancement of a dynamic transfer of charge along the B–C bond under pressure, which indicates that the ionic electrostatic interactions become stronger. Our work demonstrates the existence of pressure-induced ferroelectrics and thus provides opportunities to design devices with ferroelectrics working on high-pressure conditions.

DOI: [10.1103/PhysRevB.106.174106](https://doi.org/10.1103/PhysRevB.106.174106)

I. INTRODUCTION

Ferroelectric materials are one of typical functional materials having wide technological applications. There is a ferroelectric structure transition from a nonpolar high-symmetry phase to a polar phase. The electric polarization of a ferroelectric can be switched by an applied electric field. Many ferroelectrics have been discovered including perovskite oxides ABO_3 , hexagonal ABC [1], diatomic GeTe and PbS (distorted NiAs-type structure), two-dimensional ferroelectrics [2], and so on [3]. It is generally believed that ferroelectricity is typically suppressed under hydrostatic compression [3]. In 1975, a classical work on this topic was published by Samara *et al.* [4]. They found that the transition temperature decreases with hydrostatic pressure for displacive phase transitions with soft zone-center phonons in perovskites with no known exceptions at that time. They also expected that the transition temperature may vanish under sufficiently high pressure. From then on, much effort has been expended to investigate ferroelectrics under pressure.

Pressure-induced ferroelectricity in $(NH_4)_3H(SO_4)_2$ was discovered by Gesi in 1977 [5]. Two ferroelectric phases were found and a two-sublattice model was proposed to explain dielectric properties influenced by the pressure. High-pressure Raman study on $PbTiO_3$ has been carried out and a tricritical point in the (P, T) phase diagram was found [6]. Initially, $PbTiO_3$ was predicted to violate Samara's theory [7]. However, experimental results revealed that there were complex structural phase transitions for $PbTiO_3$ under pressure [8]. In the ferroelectric $PbMg_{1/3}Ta_{2/3}O_3$, the lead displacement was found to decrease under pressure [9]. For

$BiFeO_3$, six phase transitions from the ferroelectric phase to nonpolar phases were reported experimentally [10]. The transitions from the $R3m$ polar phase to monoclinic polar phases were reported in $PbFe_{0.5}Nb_{0.5}O_3$ [11]. Different from conventional multiferroics, magnetoelectric coupling and polar phases were not suppressed under pressure. A reentrant ferroelectric phase in the superlattice $(Pb_{0.5}Bi_{0.5})(Ti_{0.5}Fe_{0.5})O_3$ above 7 GPa was reported by Singh *et al.* [12]. Pressure-induced multiferroics $RMnO_3$ (R is a rare-earth ion) were predicted [13]. Pseudo Jahn-Teller effects were considered to be reasons for induced spontaneous polarization in $RMnO_3$. In 2021, experimental works by Deemyad *et al.* proved that a polar metal emerges in a pressure-induced ferroelectric-like transition for antiperovskites $Hg_3Te_2X_2$ ($X = Cl, Br$) [14]. The band gap of $Hg_3Te_2Br_2$ closed from 2.5 eV to metallic polar state. From the viewpoint of fundamental physics, ferroelectrics (insulators or semiconductors) may be induced by pressure.

In this work, we firstly set up a general phenomenological theory to describe pressure-induced ferroelectric transitions in which ferroelectrics are created. This theory allows us to get main physical features of such structure transition driven by pressure. Then, we identify a previously unrecognized hexagonal ABC ferroelectric material LiBC in the LiGaGe structure type with the $P6_3mc$ symmetry [1] induced by high pressure (~ 108 GPa) as calculated in Ref. [15] through global structural minimization. At ambient pressure, LiBC is in the nonpolar state with the $P6_3/mmc$ ZrBeSi structure type. High pressure drives it into the polar state. With the help of first-principles calculations, we study the physical mechanism of the structure transition from the nonpolar phase to the polar phase under pressure. The ferroelectric multiple-well energy is found for LiBC different from the characteristic double-well energy for typical ferroelectrics. The softness of one

*zhanghu@hbu.edu.cn

of the A_{2u} modes above 60 GPa is discovered, which is the key issue to understand the pressure-induced ferroelectric transition. Born effective-charge, dielectric- and piezoelectric responses are also investigated. The relations between the behavior of LiBC and our phenomenological theory are analyzed.

II. METHODOLOGY

To study physical properties of real materials under high pressure, we have performed first-principles calculations based on density-functional theory [16] with the Perdew-Burke-Ernzerhof functional in generalized gradient approximation (GGA) [17] in the Vienna *Ab initio* Simulation Package (VASP) [18–20]. We used a $12 \times 12 \times 12$ Monkhorst-Pack grid [21] and an energy cutoff of 650 eV. The crystal structures were relaxed until the Hellmann-Feynman forces were less than 1 meV/Å. The Berry phase method [22] was used to calculate the electric polarization. The Heyd-Scuseria-Ernzerhof (HSE) hybrid functional [23] was used to obtain the electronic band structures.

III. RESULTS AND DISCUSSION

A. Phenomenological theory

By analogy to the Landau-Devonshire theory [3] describing the transition from a paraelectric phase to a ferroelectric phase with the decrease of temperature, we now set up a phenomenological theory to describe the high-pressure induced ferroelectrics. We choose the origin of enthalpy for the nonpolar structure to be zero, and thus we write enthalpies as

$$H_u = \frac{1}{2}au^2 + \frac{1}{4}bu^4 + \frac{1}{6}cu^6 + \dots, \quad (1)$$

where u is the polar distortion. We use the more general parameters polar distortion, not the electric polarization, since it is hard to define polarization for polar metals. Hence, this phenomenological theory can also be used to describe metallic phases. We assume that around the critical pressure ($P \sim P_0$)

$$a = a_0(P - P_0), \quad (2)$$

and the other coefficients in the enthalpy expansion are independent of pressure. Considering the linear pressure dependence of a , we have the general expression for the enthalpy:

$$H_u = \frac{1}{2}a_0(P - P_0)u^2 + \frac{1}{4}bu^4 + \frac{1}{6}cu^6 + \dots. \quad (3)$$

According to the reality in materials, c is positive.

The sign of the coefficient b determines the nature of the paraelectric-ferroelectric transition under pressure. If $b > 0$, the enthalpy will evolve continuously as a function of increasing pressure as shown in Fig. 1(a). For $P < P_0$, the nonpolar structure is in the global minimum and thus the structure is in the paraelectric phase. There is a transition at $P = P_0$. For $P > P_0$, there are minima at finite u , which indicate that the polar structure is in the global minimum and thus the structure is in the ferroelectric phase. This case is similar to the second-order phase transition driven by temperature [3].

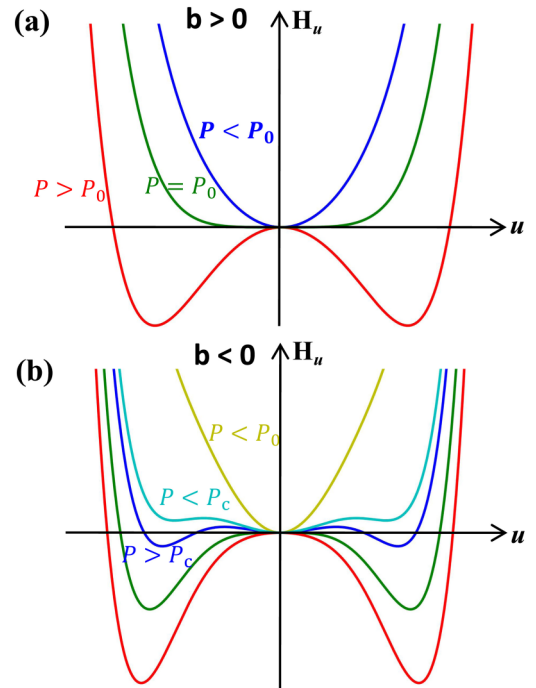


FIG. 1. Enthalpy as a function of the polar distortion u for (a) $b > 0$ and (b) $b < 0$.

If $b < 0$, it is clear that even if $P > P_0$ the enthalpy may still have a subsidiary minimum at nonzero u . As the pressure is enhanced, this minimum will drop in enthalpy below that of the nonpolar state, and so will be the dynamically favored state. The pressure at which this happens is the critical pressure P_c , which now exceeds P_0 . At any pressure between P_c and P_0 the nonpolar state exists as a local minimum of the enthalpy. This situation is shown in Fig. 1(b). This type of phase transition under pressure is similar to the first-order phase transition driven by temperature. There is also hysteresis for ferroelectrics as shown schematically in Fig. 2. The polarization will not be immediately switched due to the barrier between different minima for $P > P_0$. This behavior can be checked experimentally.

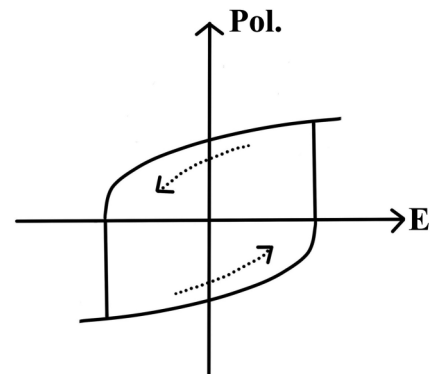


FIG. 2. Schematic picture of hysteresis in ferroelectric crossing critical points.

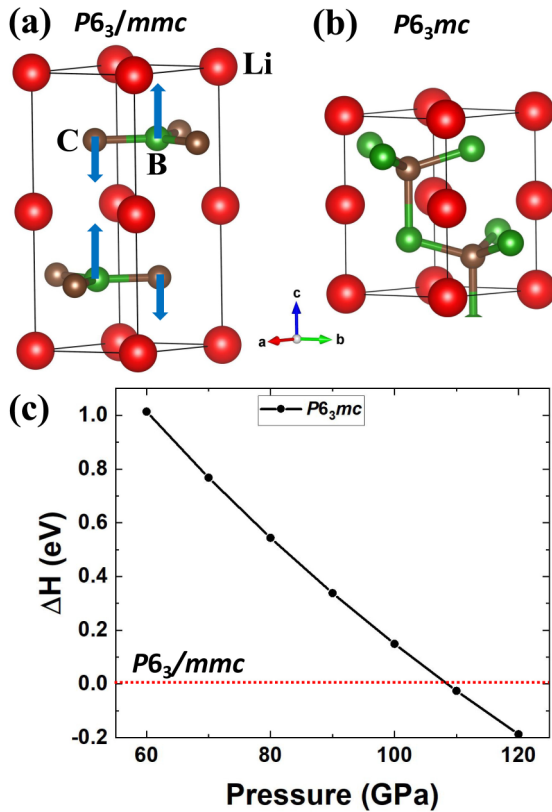


FIG. 3. (a) Crystal structure of the nonpolar LiBC with the $P6_3/mmc$ ZrBeSi structure type at ambient pressure. Arrows indicate the displacement of one of the A_{2u} modes. (b) The crystal structure of the polar LiBC with the $P6_3mc$ LiGaGe structure type at 110 GPa. (c) Enthalpies of the polar phase relative to the nonpolar phase as a function of pressure.

B. High-pressure induced ferroelectric LiBC

At ambient pressure, the nonpolar state of LiBC has the $P6_3/mmc$ ZrBeSi structure type as shown in Fig. 3(a). The Li, B, and C atoms site at the $2a$, $2c$, and $2d$ Wyckoff positions, respectively. The calculated crystal-structure parameters are $a = 2.749 \text{ \AA}$ and $c = 7.035 \text{ \AA}$, which are consistent with experimental results ($a = 2.714 \text{ \AA}$ and $c = 7.146 \text{ \AA}$) [24]. The polar phase of LiBC has the $P6_3mc$ LiGaGe structure type with Li, B, and C atoms sitting at the $2a$, $2b$, and $2b$ Wyckoff positions, respectively, as shown in Fig. 3(b). Through careful structure relaxation we find that the initial input polar structure of LiBC is always relaxed to the nonpolar structure below 60 GPa and thus we cannot obtain the polar structure, which indicates the instability of the polar structure. Above 60 GPa (before the structural transition), the polar LiBC is a metastable phase since its enthalpy is higher than that of the nonpolar structure. In Fig. 3(c), we show the enthalpies' difference between the polar phase and the nonpolar phase as a function of pressure. From this we know that the phase transition pressure is about 108 GPa. The calculated crystal-structure parameters for the polar LiBC at 110 GPa are $a = 2.690 \text{ \AA}$ and $c = 4.356 \text{ \AA}$ with Wyckoff positions of Li $2a$ (0, 0, 0.045), B $2b$ (1/3, 2/3, 0.843), and C $2b$ (1/3, 2/3, 0.239). Thus, the lattice constant c is highly reduced by pressure.

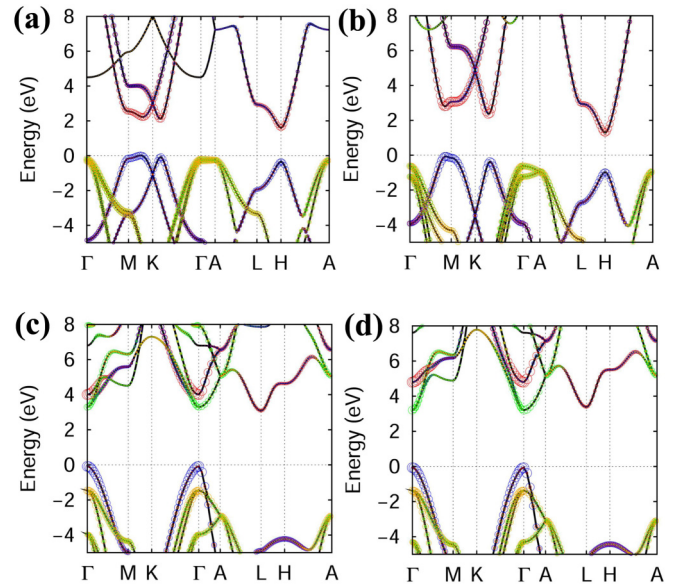


FIG. 4. The energy band structures of the nonpolar LiBC at (a) ambient pressure and (b) 100 GPa. The energy band structures of the polar LiBC at (c) 60 GPa and (d) 110 GPa. The color lines indicate the projection to the B p_z (red), C p_z (blue), B $p_{x/y}$ (green), and C $p_{x/y}$ (orange) states.

The HSE electronic structures of nonpolar LiBC at ambient pressure are shown in Fig. 4(a), which indicates that nonpolar LiBC is a semiconductor with an energy gap of 1.59 eV. In the M - K direction, the C - p_z and B - p_z orbitals occupy the top of valence bands and the bottom of the conduction bands, respectively. They form the intralayer π bonding. In the Γ - A direction, there are nearly flat bands at the top of valence bands having sp^2 -hybridized σ -bonding character. For valence bands at the Γ point, the σ bands contributed with $p_{x/y}$ orbitals are separated into two classes. The top one is twofold degenerate with intralayer antibonding and interlayer antibonding. The lower one is also twofold degenerate with intralayer antibonding and interlayer bonding. The splitting of these bands is very small due to the weaker interlayer coupling. At the Γ point, four π bands contributed from p_z orbitals locate below the σ bands. The lower one is intralayer bonding and interlayer bonding (mixing with Li- s orbital). The top one is intralayer bonding and interlayer antibonding (no mixing with Li- s orbital). Since the p_z orbital is along the c direction, the interlayer coupling is larger than that of the σ bands. Thus, the splitting of π bands is relatively large. Intuitive pictures of these bonding and antibonding characters are shown in Fig. 5. From the electronic structures of nonpolar LiBC at 100 GPa (with an energy gap of 1.36 eV) showing in Fig. 4(b), we can find that the σ -bonding states are no longer flat and drop in energy compared to the top of valence bands.

The nearly flat bands (weak dispersions) in Fig. 4(a) indicate the two-dimensional feature of these bands. From the atomic structures of nonpolar LiBC at ambient pressure, we know that the B and C form two-dimensional planar hexagons separated by Li layers. The lattice constant c is 7.035 \AA . The distance between each B-C layers is 3.517 \AA , which is significantly larger than the length (1.587 \AA) of the B-C bond

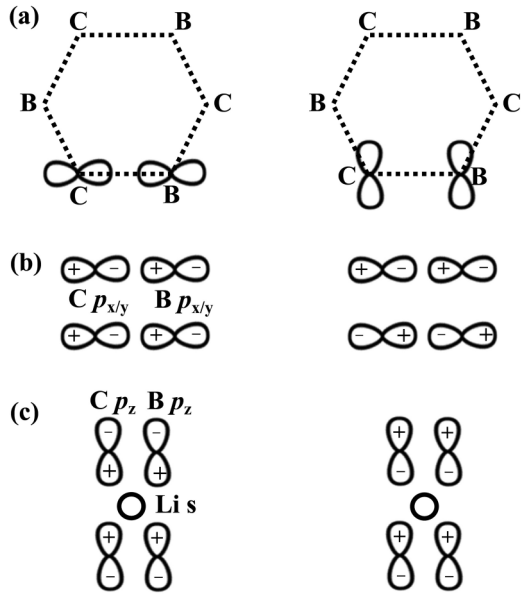


FIG. 5. Schematic pictures of bonding characters in nonpolar LiBC. (a) σ bonding (left) and π bonding (right) in two-dimensional planar B-C hexagons. (b) Intralayer antibonding and interlayer bonding (left); intralayer antibonding and interlayer antibonding (right). (c) Intralayer bonding and interlayer bonding (left); intralayer bonding and interlayer antibonding (right).

in each planar B-C layer. Obviously, bonding between each planar B-C layers is very weak due to their large distances. The nearly flat bands in the Γ -A direction come from the B-C bonding in each planar B-C layer and have nearly no contributions from bonding between planar B-C layers along the c direction. In a word, the two-dimensional σ -bonding character in nonpolar LiBC at ambient pressure results in nearly flat bands in the Γ -A direction at the top of valence bands. At 100 GP, the lattice constant c is 5.369 Å. The distance between each B-C layer is 2.684 Å, which is highly reduced compared to the value of 3.517 Å for nonpolar LiBC at ambient pressure. In this case, there is weak bonding between each planar B-C layer. The bands in the Γ -A direction at the top of valence bands shown in Fig. 4(b) have contributions from bonding between planar B-C layers along the c direction. These bands have now lost two-dimensional features and have weak three-dimensional features and thus are no longer flat anymore.

The polar LiBC at 60 GPa is a semiconductor with an energy gap of 3.16 eV as can be found in Fig. 4(c). At the Γ point, the C- p_z orbitals occupy the top of valence bands and the C- $p_{x/y}$ orbitals locate just below C- p_z orbitals. The B- $p_{x/y}$ orbitals occupy the bottom of the conduction bands. In the Γ -A direction, the C- p_z bands crosses the C- $p_{x/y}$ bands. The band gap of polar LiBC at 110 GPa is 3.27 eV as shown in Fig. 4(d). At high pressure, the polar LiBC has a larger energy gap than that of nonpolar LiBC, which indicates that the bonding hybridization in polar states is stronger. From these we know that, with the increase of pressure, sp^3 -like hybridized bonding is more favorable than sp^2 -hybridized σ bonding in LiBC. The reasons for this result are connected

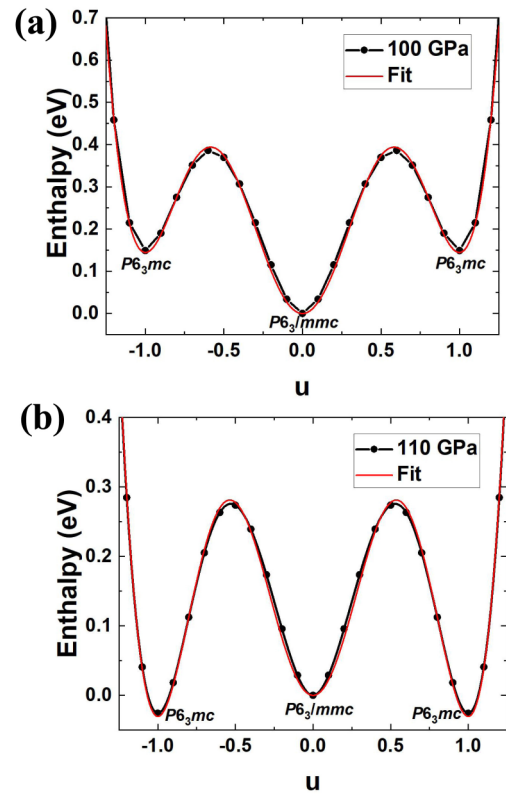


FIG. 6. Multiple-well energy of LiBC as a function of polar distortion obtained by linear interpolation between the polar and nonpolar structures at (a) 100 GPa and (b) 110 GPa. Red lines indicate the fitting data with the phenomenological theory.

with the dynamic charge transfer and will be discussed in the next section.

Figures 6(a) and 6(b) shows the multiple-well energy of LiBC as a function of polar distortion obtained by linear interpolation between the polar $P6_3/mc$ and nonpolar $P6_3/mmc$ structures at 100 and 110 GPa. The polar phase locates at a local minimum at 100 GPa. Remarkably, there is a saddle point between the nonpolar and polar structures. The ferroelectric multiple-well energy of LiBC shown in Fig. 6(b) is very different from the characteristic double-well energy of typical ferroelectrics such as NaMgP [1]. This indicates the specificity of the ferroelectric LiBC driven by high pressure. The multiple-well energy in Fig. 6(b) is similar to the case of $b < 0$ for the phenomenological theory shown in Fig. 1(b). We have fitted our first-principles results with the phenomenological theory given in Eq. (3). Results are given in red lines in Fig. 6. The polar distortion (dimensionless) $u = 1$ corresponds to the polar phase. For the ferroelectric LiBC, we obtain $a_0 = 2.29$ eV/GPa, $b = -23.48$ eV, and $c = 29.77$ eV and higher-order terms with -13.13 and 2.25 eV for u^8 and u^{10} , respectively. Obviously, a negative value of b is obtained. The physical mechanisms of the formation of multiple-well energy curves are related to phonon modes and will be discussed in the next section.

In Fig. 6(b) we can also find that the energy barrier between the polar state and the nonpolar reference state is about 0.3 eV. This value is comparable to those of known ferroelectrics

TABLE I. Buckling parameters d and dielectric coefficients in polar LiBC at various pressure.

Pressure (GPa)	d (Å)	ϵ_{11} (Ionic)	ϵ_{33} (Ionic)	ϵ_{11} (Ion clamped)	ϵ_{33} (Ion clamped)
60	0.461	1.62	3.74	6.76	8.14
70	0.460	1.56	3.38	6.73	7.89
80	0.459	1.52	3.13	6.71	7.72
90	0.457	1.47	2.93	6.70	7.59
100	0.455	1.43	2.78	6.68	7.48
110	0.453	1.40	2.65	6.67	7.40
120	0.451	1.37	2.54	6.66	7.33

BaTiO₃ (0.02 eV) and PbTiO₃ (0.2 eV) [3]. The barriers of theoretically predicted ferroelectrics LiBeSb and LiZnSb are 0.58 and 0.80 eV, respectively [1]. These results illustrate the possibility of realistic switching of LiBC. The computed polarization of LiBC at 110 GPa is 1.95 C/m², which is much larger than those of LiBeSb (0.59 C/m²) and LiZnSb (0.56 C/m²) [1]. This is due to the strong buckling of the C-B plane in the polar structure. The buckling parameter, d , can be defined as the distance along the c axis between the inequivalent B and C atoms in the buckled plane. At 110 GPa, we have $d = 0.453$ Å. The typical value of d for other hexagonal ABC ferroelectrics is 0.1 Å. An extremely large d in LiBC leads to a large polarization. This is one of the characteristics of the high-pressure induced ferroelectric LiBC. In Table I we show buckling parameters d as a function of pressure. The change of d is rather small. Therefore, the polar structure of LiBC always accompanies a large buckling parameter.

C. Physical mechanisms of ferroelectric transitions

In this part, we investigate the physical mechanisms of the high-pressure induced ferroelectric transitions in LiBC based on the soft-mode theory, which is important to understand ferroelectricity [3]. For the paraelectric nonpolar phase, the lowest-frequency polar phonon mode as a function of temperature becomes softer and finally goes to zero frequency. First-principles calculations give an unstable polar phonon in the nonpolar reference structure. In the cubic perovskite structure (e.g., BaTiO₃) the unstable polar mode (imaginary frequencies) is one of three optical T_{1u} modes. A double-well energy as a function of distortion amplitude is obtained by freezing the atomic displacement pattern of the unstable mode. However, we obtain a multiple-well energy for LiBC at high pressure. Thus, we can expect that the behavior of polar phonon mode in LiBC at high pressure may be strange.

From the factor group analysis, we know that the nonpolar LiBC with $P6_3/mmc$ symmetry have three acoustic modes and 15 optical modes at the Brillouin-zone center. Optical modes can be expressed as

$$2A_{2u} + B_{2u} + 2E_{1u} + 2E_{2g} + E_{2u}, \quad (4)$$

where the two E_{2g} modes are Raman active; $2E_{1u}$ and $2A_{2u}$ modes are infrared active. One of the A_{2u} modes, that B and C sublattices move against each other along c [see arrows in Fig. 3(a)] and Li not at rest, is related to the structural transition from the nonpolar to polar phases under high

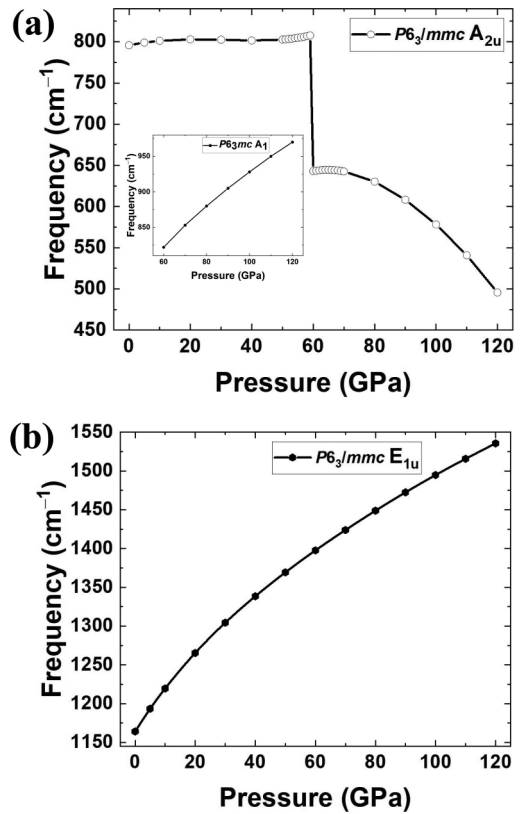


FIG. 7. Frequencies of the (a) A_{2u} and (b) E_{1u} models as a function of pressure in nonpolar LiBC. The inset shows frequencies of the A_1 mode as a function of pressure in polar LiBC.

pressure. At ambient pressure, our calculated frequency of this model is 795 cm⁻¹ which is consistent with experimental data (825 cm⁻¹) [25]. This phonon mode is polarized along the c direction with the calculated displacement eigenvector of $[[0, 0, +0.121], [0, 0, -0.549], \text{ and } [0, 0, +0.428]]$ for Li, B, and C. In Fig. 7(a) we show frequencies of this model as a function of pressure. Below 60 GPa, the frequency changes very slowly. There is a discontinuity at 60 GPa. Above 60 GPa, the frequency decreases with the increase of pressure. The softness of this phonon mode indicates a structural transition from the nonpolar to polar phases and will be further explained below. The calculated displacement eigenvectors (for Li, B, and C) at 100 and 110 GPa are $[[0, 0, +0.174], [0, 0, +0.425], [0, 0, -0.537]]$, and $[[0, 0, +0.144], [0, 0, +0.443], [0, 0, -0.531]]$, respectively. Evidently, the pressure also changes displacement eigenvectors. For comparison, we plot frequencies of one of the E_{1u} models (B–C bond stretching mode, odd displacement of BC layers) as a function of pressure in Fig. 7(b). Obviously, the frequency always increases with the increasing of pressure. The hardening of this mode is related to the reduction of cell parameters under high pressure. Therefore, the property of the frequencies of the A_{2u} mode under high pressure is significant different from that of the E_{1u} mode.

With the help of the behavior of A_{2u} modes under high pressure, the formation of the multiple-well energy curves shown in Fig. 6 can be understood as follows. From Fig. 7(a), we can know that the frequencies for one of the A_{2u} modes

TABLE II. Frequencies of the zone-center phonon modes in polar LiBC at 110 GPa.

Model	Frequency (cm ⁻¹)	Model	Frequency (cm ⁻¹)
<i>E</i> 1	1208	<i>A</i> 1	950
<i>E</i> 2	1205	<i>B</i> 1	853
<i>B</i> 1	1090	<i>E</i> 2	818
<i>E</i> 1	1026	<i>A</i> 1	807
<i>B</i> 1	960	<i>E</i> 2	667

decrease with the increase of pressure above 60 GPa. This indicates the change of the structural stability of the nonpolar LiBC. The frequencies are 578 and 540 cm⁻¹ for 100 and 110 GPa, respectively. These values are reduced significantly compared to the frequency of 795 cm⁻¹ at ambient pressure. But, it is known that first-principles calculations give imaginary frequencies (usually denoted as negative values) for unstable modes for typical ferroelectrics (such as BaTiO₃ and PbTiO₃). For nonpolar LiBC under high pressure, the frequencies of the soft mode are highly reduced but still remain large even around the phase transition pressure compared to phonon modes with imaginary frequencies in typical ferroelectrics. This suggests that nonpolar LiBC still retains its structural stability to some extent. For typical ferroelectrics, first-principles calculations give the double-well energy curve, in which the nonpolar state is a *local maximum* similar to the case in Fig. 1(a) for $P > P_0$ with $b > 0$. In Fig. 6, we can find that the nonpolar state LiBC is a *local minimum*, not a *local maximum*. This indicates that nonpolar LiBC under high pressure still retains its structural stability, which is consistent with the large frequencies (> 500 cm⁻¹) of the soft mode different from typical ferroelectrics with imaginary frequencies. Such results also agree with the negative value of b obtained by fitting our first-principles results with the phenomenological theory. For both the nonpolar and polar states of LiBC under high pressure, we have a *local minimum*, which results in multiple-well energy curves. However, for typical ferroelectrics, the nonpolar state is a *local maximum* and the polar state is a *local minimum*, which results in double-well energy curves. These are reasons of the formation of multiple-well energy curves for LiBC.

Similar to the nonpolar phase, the zone-center phonon modes for polar LiBC with $P6_3mc$ symmetry are 3 acoustic modes and 15 optical modes that can be expressed as

$$2A_1 + 3B_1 + 3E_2 + 2E_1, \quad (5)$$

where the two A_1 modes are both Raman active and infrared active, and $3E_2$ modes are Raman active. Calculated phonon frequencies at 110 GPa are shown in Table II. One of the A_1 modes that B and C sublattices move against each other along c is related to the A_{2u} mode of the nonpolar structure LiBC. The calculated displacement eigenvector for this A_1 mode at 60 GPa is $[[0, 0, -0.271], [0, 0, +0.564], \text{ and } [0, 0, -0.328]]$ for Li, B, and C. The inset in Fig. 7(a) shows frequencies of this A_1 mode as a function of pressure. Clearly, the frequency always increases with the increase of pressure. The hardening of this mode is very different from that of the A_{2u} mode. Our calculated displacement eigenvectors (for Li, B, and C) at

100 and 110 GPa are $[[0, 0, -0.163], [0, 0, +0.557], [0, 0, -0.403]]$, and $[[0, 0, -0.149], [0, 0, +0.554], [0, 0, -0.411]]$, respectively. These behaviors of phonon under high pressure are the physical mechanism of the structural transition from the nonpolar to polar phases.

For ferroelectrics, the Born effective charges and dielectric responses are useful to further understand the ferroelectric transitions from a different view point. The Born effective-charge tensors are related to the coupling of a macroscopic field with relative sublattice displacements (zone-center phonons) in crystals. They can provide insight into ferroelectric phenomena and be defined as the first derivative of polarization with atomic displacement [3]:

$$Z_{s,\alpha\beta}^* = \frac{\Omega}{e} \frac{\partial P_\alpha}{\partial u_{s,\beta}}, \quad (6)$$

where Ω is the primitive cell volume and $e > 0$ is the charge quantum. The Born charges in ferroelectric perovskites are strongly anomalous. For KNbO₃, Z_s^* for K, Nb, O1, and O2 are 0.8, 9.1, -6.6, and -1.7, respectively. The Nb and O1 values are much larger than their nominal static charges (5 and -2). The Born charges of atoms in LiBC have two independent components due to its crystal symmetry. The nominal static charges of Li, B, and C are 1, 3, and -4, respectively. At ambient pressure, the calculated Born charges in nonpolar LiBC are $Z_{Li,11}^* = 0.82$, $Z_{Li,33}^* = 1.46$, $Z_{B,11}^* = 2.34$, $Z_{B,33}^* = 0.34$, $Z_{C,11}^* = -3.16$, and $Z_{C,33}^* = -1.80$. These values show strong anisotropy. At 110 GPa, the Born charges in nonpolar LiBC are $Z_{Li,11}^* = 0.79$, $Z_{Li,33}^* = 1.15$, $Z_{B,11}^* = 2.89$, $Z_{B,33}^* = 3.35$, $Z_{C,11}^* = -3.68$, and $Z_{C,33}^* = -4.50$, which indicates that all of $Z_{s,33}^*$ are slightly larger than their corresponding nominal static charges. In Fig. 8(a) we show the Born charges of C as a function of pressure for the nonpolar structures LiBC. $Z_{C,33}^*$ is easier to be influenced by the pressure than that of $Z_{C,11}^*$. This is related to structure distortion ability along the c axis in nonpolar LiBC under pressure. On the other hand, the Born charges in polar LiBC at 110 GPa are $Z_{Li,11}^* = 0.96$, $Z_{Li,33}^* = 0.95$, $Z_{B,11}^* = 0.86$, $Z_{B,33}^* = 1.01$, $Z_{C,11}^* = -1.82$, and $Z_{C,33}^* = -1.96$. Compared to values of nonpolar phase at 110 GPa, $Z_{s,33}^*$ are all reduced significantly. Born charges of C as a function of pressure for the polar LiBC are shown in Fig. 8(b). Different from the case in nonpolar LiBC, the change of $Z_{C,11}^*$ and $Z_{C,33}^*$ is very small. These results reveal different Born charge properties between nonpolar and polar structures.

There is a close connection between Born charges and the softness of the A_{2u} mode. The soft zone-center mode frequency ω_s is given by the difference between a short-range (SR) interaction and a long-range (LR) interaction [4]:

$$\omega_s^2 \propto [\text{SR interaction}] - [\text{LR interaction}]. \quad (7)$$

The ionic electrostatic interactions are long range (which favor the polar ferroelectric state), while covalent interactions tend to be short range (which favor the nonpolar state) [14]. From above discussions we know that the Born charges $Z_{s,33}^*$ in nonpolar LiBC can be easily changed by pressure and are slightly larger than their corresponding nominal static charges at 110 GPa. The large values of $Z_{C,33}^*$ and $Z_{B,33}^*$ (responsible for the strong long-range Coulomb interaction) are mainly produced by an enhancement of a dynamic transfer of charge

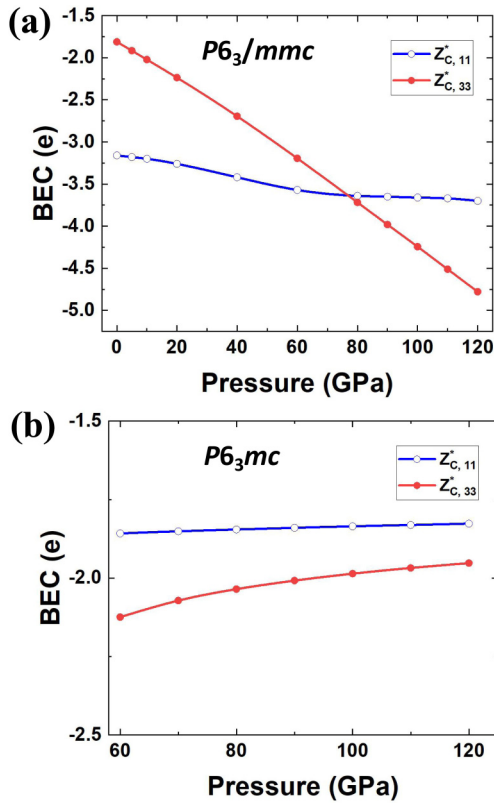


FIG. 8. Born charges $Z_{C,\alpha\beta}^*$ as a function of pressure for the (a) nonpolar and (b) polar LiBC.

along the B–C bond under pressure. Therefore, the covalent bonds become weaker while the ionic electrostatic interactions become stronger under higher pressure. Based on (7), this explains the softness of the A_{2u} mode shown in Fig. 7(a) and thus gives the physical mechanism of the high-pressure induced ferroelectrics. As a result, the two-dimensional planar B–C layers (sp^2 -hybridized σ bonding) become strongly puckered B–C layers forming three-dimensional B–C framework results in sp^3 -like hybridized bonding. These are the reasons why sp^3 -like hybridized bonding is more favorable than sp^2 -hybridized σ bonding in LiBC with the increase of pressure.

The dielectric coefficients in LiBC have two independent components determined by its crystal symmetry. In Fig. 9 we plot the pressure-dependent dielectric coefficients for the nonpolar LiBC. For the ion-clamped contribution, the change of ϵ_{11} is very small with the increase of pressure, while ϵ_{33} increases exponentially above 60 GPa. For the ionic contribution, ϵ_{33} changes linearly and ϵ_{11} changes nonlinearly. The dielectric coefficients in polar LiBC are given in Table I. The pressure does not induce significant changes for dielectric coefficients. The piezoelectric coefficient is $d_{33} = 1.28 \text{ C/m}^2$. These results can be compared with future experimental results.

Finally, based on above results, we explain the fact that we can only find the $P6_3mc$ phase for LiBC under pressure. Below 60 GPa, we have tested the $P6_3mc$ phase. Through careful structure relaxation we find that the initial input polar $P6_3mc$ structure of LiBC is always relaxed to the nonpolar

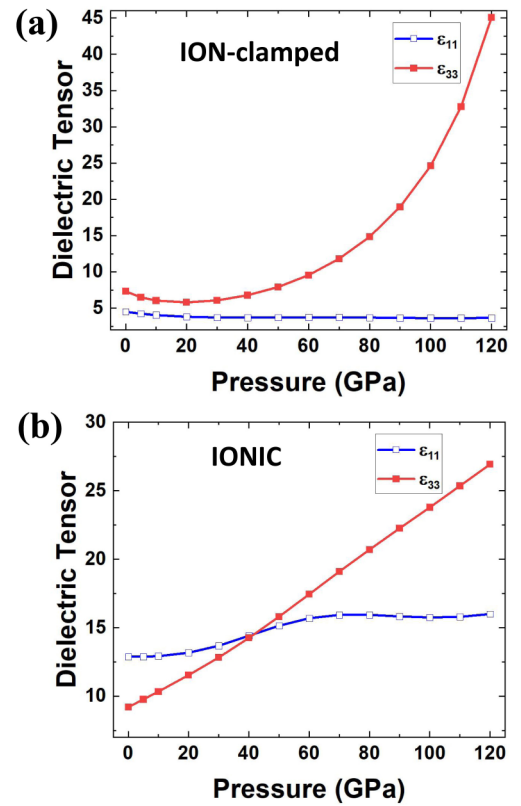


FIG. 9. (a) Ion-clamped contributions and (b) ionic dielectric coefficients as a function of pressure in nonpolar LiBC.

$P6_3/mmc$ structure. This indicates that the nonpolar LiBC is rather stable below 60 GPa, which is consistent with the slow changes of the A_{2u} mode below 60 GPa as shown in Fig. 7(a). Above 60 GPa, the frequency decreases with the increase of pressure. This A_{2u} mode, that B and C sublattices move against each other along c and Li not at rest, suggests a structural transition from the nonpolar phase to the polar $P6_3mc$ phase under high pressure. The frequencies of other modes always increase with the increasing of pressure. On the other hand, both the calculated Born charges $Z_{s,33}^*$ and dielectric coefficients ϵ_{33} can be easily influenced by pressure as shown in Fig. 8 and Fig. 9, which also suggests the structural instability along the c direction. Together these results determine the only possible structural transition in which B and C sublattices move against each other along c . Thus, we can only find the polar $P6_3mc$ phase for LiBC under pressure.

IV. CONCLUSIONS

In summary, we have set up a phenomenological theory to describe pressure-induced ferroelectrics. Based on first-principles calculations, we identify a ferroelectric transition for LiBC from the nonpolar $P6_3/mmc$ ZrBeSi structure to the polar LiGaGe structure type with the $P6_3mc$ symmetry at about 108 GPa. This pressure-induced ferroelectric transition is related to the softness of one of the A_{2u} modes above 60 GPa. An enhancement of a dynamic transfer of charge along the B–C bond under pressure is discovered, which indicates that covalent bonds and ionic electrostatic interactions

become weaker and stronger, respectively, with increasing of pressure. Dielectric and piezoelectric response properties are also investigated.

ACKNOWLEDGMENTS

This work was supported by the Advanced Talents Incubation Program of the Hebei University (Grants No.

521000981423, No. 521000981394, No. 521000981395, and No. 521000981390), the Natural Science Foundation of Hebei Province of China (Grants No. A2021201001 and No. A2021201008), the National Natural Science Foundation of China (Grants No. 12104124, No. 11904154, and No. 51772297), and the high-performance computing center of Hebei University.

-
- [1] J. W. Bennett, K. F. Garrity, K. M. Rabe, and D. Vanderbilt, Hexagonal ABC Semiconductors as Ferroelectrics, *Phys. Rev. Lett.* **109**, 167602 (2012).
- [2] R. Fei, W. Kang, and L. Yang, Ferroelectricity and Phase Transitions in Monolayer Group-IV Monochalcogenides, *Phys. Rev. Lett.* **117**, 097601 (2016).
- [3] K. Rabe, C. H. Ahn, and J.-M. Triscone, *Physics of Ferroelectrics: A Modern Approach* (Springer, Heidelberg, 2007).
- [4] G. A. Samara, T. Sakudo, and K. Yoshimitsu, Important Generalization Concerning the Role of Competing Forces in Displacive Phase Transitions, *Phys. Rev. Lett.* **35**, 1767 (1975).
- [5] K. Gesi, Pressure-induced ferroelectricity in $(\text{NH}_4)_3\text{H}(\text{SO}_4)_2$, *J. Phys. Soc. Jpn.* **43**, 1941 (1977).
- [6] J. A. Sanjurjo, E. López-Cruz, and G. Burns, High-pressure Raman study of zone-center phonons in PbTiO_3 , *Phys. Rev. B* **28**, 7260 (1983).
- [7] I. A. Kornev, L. Bellaiche, P. Bouvier, P. E. Janolin, B. Dkhil, and J. Kreisel, Ferroelectricity of Perovskites under Pressure, *Phys. Rev. Lett.* **95**, 196804 (2005).
- [8] P.-E. Janolin, P. Bouvier, J. Kreisel, P. A. Thomas, I. A. Kornev, L. Bellaiche, W. Crichton, M. Hanfland, and B. Dkhil, High-Pressure Effect on PbTiO_3 : An Investigation by Raman and X-Ray Scattering up to 63 GPa, *Phys. Rev. Lett.* **101**, 237601 (2008).
- [9] S. N. Gvasaliya, V. Pomjakushin, B. Roessli, T. Strässle, S. Klotz, and S. G. Lushnikov, Anomalous pressure dependence of the atomic displacements in the relaxor ferroelectric $\text{PbMg}_{1/3}\text{Ta}_{2/3}\text{O}_3$, *Phys. Rev. B* **73**, 212102 (2006).
- [10] M. Guennou, P. Bouvier, G. S. Chen, B. Dkhil, R. Haumont, G. Garbarino, and J. Kreisel, Multiple high-pressure phase transitions in BiFeO_3 , *Phys. Rev. B* **84**, 174107 (2011).
- [11] D. P. Kozlenko, S. E. Kichanov, E. V. Lukin, N. T. Dang, L. S. Dubrovinsky, H.-P. Liermann, W. Morgenroth, A. A. Kamynin, S. A. Gridnev, and B. N. Savenko, Pressure-induced polar phases in relaxor multiferroic $\text{PbFe}_{0.5}\text{Nb}_{0.5}\text{O}_3$, *Phys. Rev. B* **89**, 174107 (2014).
- [12] P. Singh, C. Upadhyay, Z. Konôpková, H.-P. Liermann, and D. Pandey, Evidence for pressure-induced polarization rotation, octahedral tilting, and reentrant ferroelectric phase in tetragonal $(\text{Pb}_{0.5}\text{Bi}_{0.5})(\text{Ti}_{0.5}\text{Fe}_{0.5})\text{O}_3$, *Phys. Rev. Mater.* **3**, 094405 (2019).
- [13] C. Xu, Y. Li, B. Xu, J. Íñiguez, W. Duan, and L. Bellaiche, Pressure-induced multiferroics via pseudo Jahn–Teller effects and novel couplings, *Adv. Funct. Mater.* **27**, 1604513 (2016).
- [14] W. Cai, J. He, H. Li, R. Zhang, D. Zhang, D. Y. Chung, T. Bhowmick, C. Wolverton, M. G. Kanatzidis, and S. Deemyad, Pressure-induced ferroelectric-like transition creates a polar metal in defect antiperovskites $\text{Hg}_3\text{Te}_2\text{X}_2$ ($X = \text{Cl}, \text{Br}$), *Nat. Commun.* **12**, 1509 (2021).
- [15] M. G. Zhang, The high-pressure semiconducting phase of LiBC, *Europhys. Lett.* **114**, 16001 (2016).
- [16] R. O. Jones, Density functional theory: Its origins, rise to prominence, and future, *Rev. Mod. Phys.* **87**, 897 (2015).
- [17] J. P. Perdew, K. Burke, and M. Ernzerhof, Generalized Gradient Approximation Made Simple, *Phys. Rev. Lett.* **77**, 3865 (1996).
- [18] G. Kresse and J. Furthmüller, Efficient iterative schemes for ab initio total-energy calculations using a plane-wave basis set, *Phys. Rev. B* **54**, 11169 (1996).
- [19] M. Gajdoš, K. Hummer, G. Kresse, J. Furthmüller, and F. Bechstedt, Linear optical properties in the projector-augmented wave methodology, *Phys. Rev. B* **73**, 045112 (2006).
- [20] J. Hafner, Ab-initio simulations of materials using VASP: Density-functional theory and beyond, *J. Comput. Chem.* **29**, 2044 (2008).
- [21] H. J. Monkhorst and J. D. Pack, Special points for Brillouin-zone integrations, *Phys. Rev. B* **13**, 5188 (1976).
- [22] R. D. King-Smith and D. Vanderbilt, Theory of polarization of crystalline solids, *Phys. Rev. B* **47**, 1651 (1993).
- [23] J. Heyd, G. E. Scuseria, and M. Ernzerhof, Hybrid functionals based on a screened Coulomb potential, *J. Chem. Phys.* **118**, 8207 (2003).
- [24] A. Lazicki, C. S. Yoo, H. Cynn, W. J. Evans, W. E. Pickett, J. Olamit, K. Liu, and Y. Ohishi, Search for superconductivity in LiBC at high pressure: Diamond anvil cell experiments and first-principles calculations, *Phys. Rev. B* **75**, 054507 (2007).
- [25] J. Hlinka, V. Železný, I. Gregora, J. Pokorný, A. M. Fogg, J. B. Claridge, G. R. Darling, and M. J. Rosseinsky, Vibrational properties of hexagonal LiBC: Infrared and Raman spectroscopy, *Phys. Rev. B* **68**, 220510(R) (2003).